LETTER

doi:10.1038/nature09748

# Single mimivirus particles intercepted and imaged with an X-ray laser

M. Marvin Seibert[1]*, Tomas Ekeberg[1]*, Filipe R. N. C. Maia[1]*, Martin Svenda[1], Jakob Andreasson[1], Olof Jönsson[1], Duško Odić[1], Bianca Iwan[1], Andrea Rocker[1], Daniel Westphal[1], Max Hantke[1], Daniel P. DePonte[2], Anton Barty[2], Joachim Schulz[2], Lars Gumprecht[2], Nicola Coppola[2], Andrew Aquila[2], Mengning Liang[2], Thomas A. White[2], Andrew Martin[2], Carl Caleman[1,2], Stephan Stern[2,3], Chantal Abergel[4], Virginie Seltzer[4], Jean-Michel Claverie[4], Christoph Bostedt[5], John D. Bozek[5], Sébastien Boutet[5], A. Alan Miahnahri[5], Marc Messerschmidt[5], Jacek Krzywinski[5], Garth Williams[5], Keith O. Hodgson[6], Michael J. Bogan[6], Christina Y. Hampton[6], Raymond G. Sierra[6], Dmitri Starodub[6], Inger Andersson[7], Saša Bajt[8], Miriam Barthelmess[8], John C. H. Spence[9], Petra Fromme[10], Uwe Weierstall[9], Richard Kirian[9], Mark Hunter[10], R. Bruce Doak[9], Stefano Marchesini[11], Stefan P. Hau-Riege[12], Matthias Frank[12], Robert L. Shoeman[13], Lukas Lomb[13], Sascha W. Epp[14,15], Robert Hartmann[16], Daniel Rolles[13,14], Artem Rudenko[14,15], Carlo Schmidt[14,15], Lutz Foucar[13,14], Nils Kimmel[17,18], Peter Holl[16], Benedikt Rudek[14,15], Benjamin Erk[14,15], André Hömke[14,15], Christian Reich[16], Daniel Pietschner[17,18], Georg Weidenspointner[17,18], Lothar Strüder[14,17,18,19], Günter Hauser[17,18], Hubert Gorke[20], Joachim Ullrich[14,15], Ilme Schlichting[13,14], Sven Herrmann[17,18], Gerhard Schaller[17,18], Florian Schopper[17,18], Heike Soltau[16], Kai-Uwe Kühnel[15], Robert Andritschke[17,18], Claus-Dieter Schröter[15], Faton Krasniqi[13,14], Mario Bott[13], Sebastian Schorb[21], Daniela Rupp[21], Marcus Adolph[21], Tais Gorkhover[21], Helmut Hirsemann[8], Guillaume Potdevin[8], Heinz Graafsma[8], Björn Nilsson[8], Henry N. Chapman[2,3] & Janos Hajdu[1]

**X-ray lasers offer new capabilities in understanding the structure of biological systems, complex materials and matter under extreme conditions[1–4]. Very short and extremely bright, coherent X-ray pulses can be used to outrun key damage processes and obtain a single diffraction pattern from a large macromolecule, a virus or a cell before the sample explodes and turns into plasma[1]. The continuous diffraction pattern of non-crystalline objects permits oversampling and direct phase retrieval[2]. Here we show that high-quality diffraction data can be obtained with a single X-ray pulse from a non-crystalline biological sample, a single mimivirus particle, which was injected into the pulsed beam of a hard-X-ray free-electron laser, the Linac Coherent Light Source[5]. Calculations indicate that the energy deposited into the virus by the pulse heated the particle to over 100,000 K after the pulse had left the sample. The reconstructed exit wavefront (image) yielded 32-nm full-period resolution in a single exposure and showed no measurable damage. The reconstruction indicates inhomogeneous arrangement of dense material inside the virion. We expect that significantly higher resolutions will be achieved in such experiments with shorter and brighter photon pulses focused to a smaller area. The resolution in such experiments can be further extended for samples available in multiple identical copies.**

Diffraction studies of crystalline samples have led to spectacular breakthroughs in physics, chemistry and biology over the past hundred years. Many important targets are difficult or impossible to crystallize, and this creates systematic blank areas in the structural sciences. X-ray lasers offer the possibility of stepping beyond X-ray crystallography, to extend structural studies to single, non-crystalline particles or molecules[1]. In this Letter, we present results on biological imaging with an X-ray free-electron laser, and bring together all the elements required for structural studies of single, non-crystalline objects.

Mimivirus (*Acanthamoeba polyphaga* mimivirus) is the largest known virus[6]. Its size is comparable to the size of the smallest living cells (in fact, the name mimivirus stands for 'microbe-mimicking virus'). The viral capsid (0.45 μm in diameter) has a pseudo-icosahedral appearance and is covered by an outer layer of dense fibrils[7,8]. The total diameter of the particle, including fibrils, is about 0.75 μm. Mimivirus is too big for a full three-dimensional reconstruction by cryo-electron microscopy[7] and its fibrils prevent crystallization. The genome[9] has 1.2 million base pairs (comparable to a small bacterium) and contains several genes previously thought to be present only in cellular organisms, including components of the protein translation apparatus. Mimivirus can be infected by a smaller virus, named a 'virophage'[10], which seems to be the first example of a virus behaving as a parasite of another virus[8]. Studies of mimivirus are causing a paradigm shift in virology and have led to renewed debates about the origin and the definition of viral and cellular life[11].

Figure 1 shows the experimental arrangement for imaging single virus particles. The sample injector, which uses aerodynamic focusing, was mounted into the CFEL-ASG Multi-Purpose (CAMP) instrument[12] on the Atomic, Molecular and Optical Science (AMO) beamline[13] at the Linac Coherent Light Source[5] (LCLS). We recorded far-field diffraction patterns at a reduced pressure ($10^{-6}$ mbar) to minimize background scattering. Mimivirus was aerosolized from a volatile buffer (250 mM ammonium acetate, pH 7.5) using a gas dynamic nebulizer[14] in a helium atmosphere. The beam of adiabatically cooled virus particles was guided through an aerodynamic lens stack (similar to the one described in ref. 15) and entered the interaction zone with an estimated velocity of 60–100 m $s^{-1}$. The particles were intercepted randomly by

[1]Laboratory of Molecular Biophysics, Department of Cell and Molecular Biology, Uppsala University, Husargatan 3 (Box 596), SE-751 24 Uppsala, Sweden. [2]Center for Free-Electron Laser Science, DESY, Notkestrasse 85, 22607 Hamburg, Germany. [3]University of Hamburg, Notkestrasse 85, 22607 Hamburg, Germany. [4]Information Génomique et Structurale, CNRS-UPR2589, Aix-Marseille Université, Institut de Microbiologie de la Méditerranée, Parc Scientifique de Luminy, Case 934, 13288 Marseille Cedex 9, France. [5]LCLS, SLAC National Accelerator Laboratory, 2575 Sand Hill Road, Menlo Park, California 94025, USA. [6]PULSE Institute, SLAC National Accelerator Laboratory, 2575 Sand Hill Road, Menlo Park, California 94025, USA. [7]Department of Molecular Biology, Swedish University of Agricultural Sciences, Uppsala Biomedical Centre, Box 590, S-751 24 Uppsala, Sweden. [8]Photon Science, DESY, Notkestrasse 85, 22607 Hamburg, Germany. [9]Department of Physics, PSF470, Arizona State University, Tempe, Arizona 85287-1504, USA. [10]Department of Chemistry and Biochemistry, Arizona State University, Tempe, Arizona 85287-1604, USA. [11]Advanced Light Source, Lawrence Berkeley National Laboratory, Berkeley, California 94720, USA. [12]Lawrence Livermore National Laboratory, 7000 East Avenue, Mail Stop L-211, Livermore, California 94551, USA. [13]Max-Planck-Institut für Medizinische Forschung, Jahnstrasse 29, 69120 Heidelberg, Germany. [14]Max Planck Advanced Study Group, Center for Free-Electron Laser Science, Notkestrasse 85, 22607 Hamburg, Germany. [15]Max-Planck-Institut für Kernphysik, Saupfercheckweg 1, 69117 Heidelberg, Germany. [16]PNSensor GmbH, Römerstrasse 28, 80803 München, Germany. [17]Max-Planck-Institut Halbleiterlabor, Otto-Hahn-Ring 6, 81739 München, Germany. [18]Max-Planck-Institut für Extraterrestrische Physik, Giessenbachstrasse, 85741 Garching, Germany. [19]Universität Siegen, Emmy-Noether Campus, Walter Flex Strasse 3, 57068 Siegen, Germany. [20]Forschungszentrum Jülich, Institut ZEL, 52425 Jülich, Germany. [21]Institut für Optik und Atomare Physik, Technische Universität Berlin, Hardenbergstrasse 36, 10623 Berlin, Germany.

*These authors contributed equally to this work.

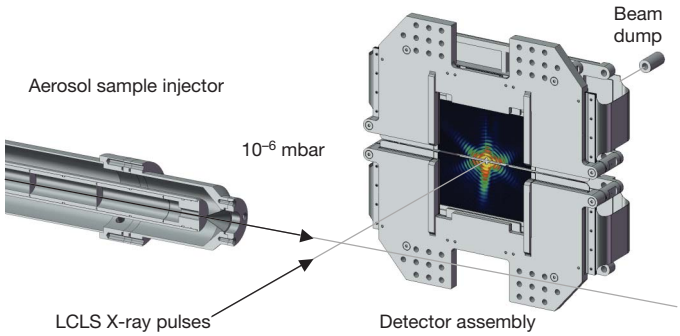


**Figure 1 | The experimental arrangement.** Mimivirus particles were injected into the pulse train of the LCLS at the AMO experimental station[13] with a sample injector built in Uppsala. The injector was mounted into the CAMP instrument[12]. The aerodynamic lens stack is visible in the centre of the injector body, on the left. Particles leaving the injector enter the vacuum chamber and are intercepted randomly by the LCLS pulses. The far-field diffraction pattern of each particle hit by an X-ray pulse is recorded on a pair of fast p–n junction charge-coupled device (pnCCD) detectors[12]. The intense, direct beam passes through an opening in the centre of the detector assembly and is absorbed harmlessly behind the sensitive detectors. Some of the low-resolution data also go through this gap and are lost in the current set-up.

the LCLS pulses. The X-ray energy was 1.80 keV (6.9-Å wavelength) and the pulse length was 70 fs (full-duration at half-maximum). The X-ray beam diameter at the interaction point was about 10 μm (full-width at half-maximum), with a maximum of $1.6 \times 10^{10}$ photons per square micrometre in the centre of this beam. This translates to a peak power density of $6.5 \times 10^{15}$ W cm$^{-2}$. Forward-scattered diffraction patterns were recorded on a pair of pnCCD detectors[12]. The direct beam exited through an opening between the two detector halves and was absorbed in a beam dump behind the detectors (Fig. 1). The detector pair was placed 564 mm away from the interaction point, giving maximum full-period resolutions of 10.2 nm at the edges and 7.2 nm at the corners of the compound detector at 1.8-keV photon energy.

Figure 2a, b shows single shot X-ray diffraction patterns of individual mimivirus particles, and Fig. 2c shows a transmission electron micrograph of a single mimivirus particle. Each of the diffraction patterns contains about 1,700,000 scattered photons. The lowest-resolution data are missing between the two detector halves, so the total number of scattered photons exceeds this number. Figure 2d, e shows autocorrelation functions calculated from the diffraction patterns. Missing low-resolution data act as a high-pass filter. For an object of extent $D$, the extent of its autocorrelation is $2D$ and the diffraction intensities are band-limited with a Nyquist rate of $1/2D$. The size and shape of the autocorrelation functions in Fig. 2d, e are indicative of hits on single virus particles. Figure 2f, g shows the reconstructed exit wavefronts for these mimivirus particles. The shapes and sizes of the reconstructed objects agree with data from prior cryo-electron microscopy studies in which 30,000 images were averaged[7]. In contrast, the reconstructed structures in Fig. 2f, g come from single shots from single particles, and demonstrate the power of this new imaging concept[1].

We performed image reconstruction by iterative phase retrieval implemented in the Hawk software package[16], using the RAAR algorithm[17] enhanced with both reality and positivity constraints. The support was handled by a Shrinkwrap algorithm[18] with the constraint of having a specific area that was estimated from the autocorrelation function. Weakly constrained modes in the reconstructions were identified and removed, using the formalism of ref. 19. This is a linear algebra method to compensate for noise, or the lack of constraints in the missing central region of the pattern. The uncertainty in the overall density was less than 10% after the identification and removal of the unconstrained modes. We then fitted these modes to match the total density of a spherical or a suitably rotated icosahedral profile. The missing modes were adjusted to give a total density that best matched the target. Residual phase fluctuations were then suppressed by averaging many reconstructions, using different random seeds. The results gave improved image reliability. For details, see Methods.

We estimated the image resolution in the reconstruction by computing the phase retrieval transfer function[2,20] (PRTF; Fig. 2h, i), which represents the confidence in the retrieved phases as a function of resolution. No consensus has emerged so far on what single PRTF value should be used as the measure of resolution (values between 0.5 and 0.1 can be found in the literature; see Methods). We characterize resolution by the point where the PRTF drops to 1/e (ref. 20), and this corresponds to a full-period resolution of 32 nm in both cases. We expect significantly higher resolutions in such experiments with shorter and brighter photon pulses focused to a smaller area.

In principle, resolution could reach less than 1 nm in a single exposure with a biological object of similar size to the mimivirus particle[3]. This resolution would require a free-electron laser pulse shorter than about 5 fs at 1.8-keV energy and a photon flux on the sample of more than $3 \times 10^{11}$ photons per square micrometre[3]. This pulse length and photon flux are beyond the initial capabilities of the LCLS, although there have already been indications of nearly transform-limited LCLS pulses lasting only a few femtoseconds and containing about $5 \times 10^{11}$ photons per pulse in the unfocused beam[21].

With very short pulses, exposures could be over before there is time for significant Auger emission or for the development of secondary electron cascades in the sample[1]. The conventional handicap of X-rays relative to electrons in imaging could thus be reversed and made into a net gain over a broad range of sample sizes. First experiments at the LCLS show a significant drop in the photoelectric cross-section of hollow atoms[22]. This effect was predicted earlier[1], but it is larger than expected and can already be measured with LCLS pulses 20–80 fs in duration[22]. The results show photoabsorption decreased 20-fold in hollow neon to equal the cross-section of coherent scattering[22]. In addition, neon ions with double core holes had an extended lifetime[22]. At 1.8-keV photon energy, more than 90% of the total photoelectric cross-section of carbon, nitrogen and oxygen can be attributed to 1*s* electrons. Ejection of these electrons at the beginning of an intense and short pulse could practically stop photoionization without significantly changing the elastic cross-sections of outer-shell electrons.

We see no measurable sample deterioration. With the X-ray pulses used in this study, the explosion of micrometre-sized objects is hydrodynamic[3] and the sample burns from the outside inwards, rarefying and destroying outer contours first. Trapped electrons move inwards to neutralize an increasingly positive core, and leave behind a positively charged outer layer, which then peels off over some picoseconds[23]. The reconstructed exit wavefront of the mimivirus particle shows well-defined outer contours and gives a sample size consistent with the intact virus capsid (we do not expect to see the thin viral fibrils at the length scales accessible here). Other studies of protein nanocrystals[24] at the LCLS at 0.9-nm resolution show no measurable deterioration of Bragg peaks during illumination with pulses similar to those used here. The size of these protein nanocrystals was similar to the size of the mimivirus particles.

At this stage, it is unclear how reproducible is the interior structure of mimivirus particles (or that of any other viral particles) in terms of atomic positions, and this will need further study. The viral inner capsid consists of a thin protein shell (about 7 nm thick) lined with phospholipid membranes. The structure of the protein shell seems to be reproducible to at least 6.5 nm resolution[7]. Figure 2d, e suggests an inhomogeneous interior structure for the virion. The interior structure does not necessarily follow the pseudo-icosahedral outer shape (the capsid is believed to have a single, five-fold symmetry axis[7]).

The penetration depth of X-rays permits studies on the interiors of large objects. The methods applied here require no modifications to the sample such as staining, freezing, sectioning, radiolabelling or crystallization, and can also be used to image cells that are alive at the time of the exposure. The amount of missing data can be reduced by adding an additional detector pair behind the first pair. Another

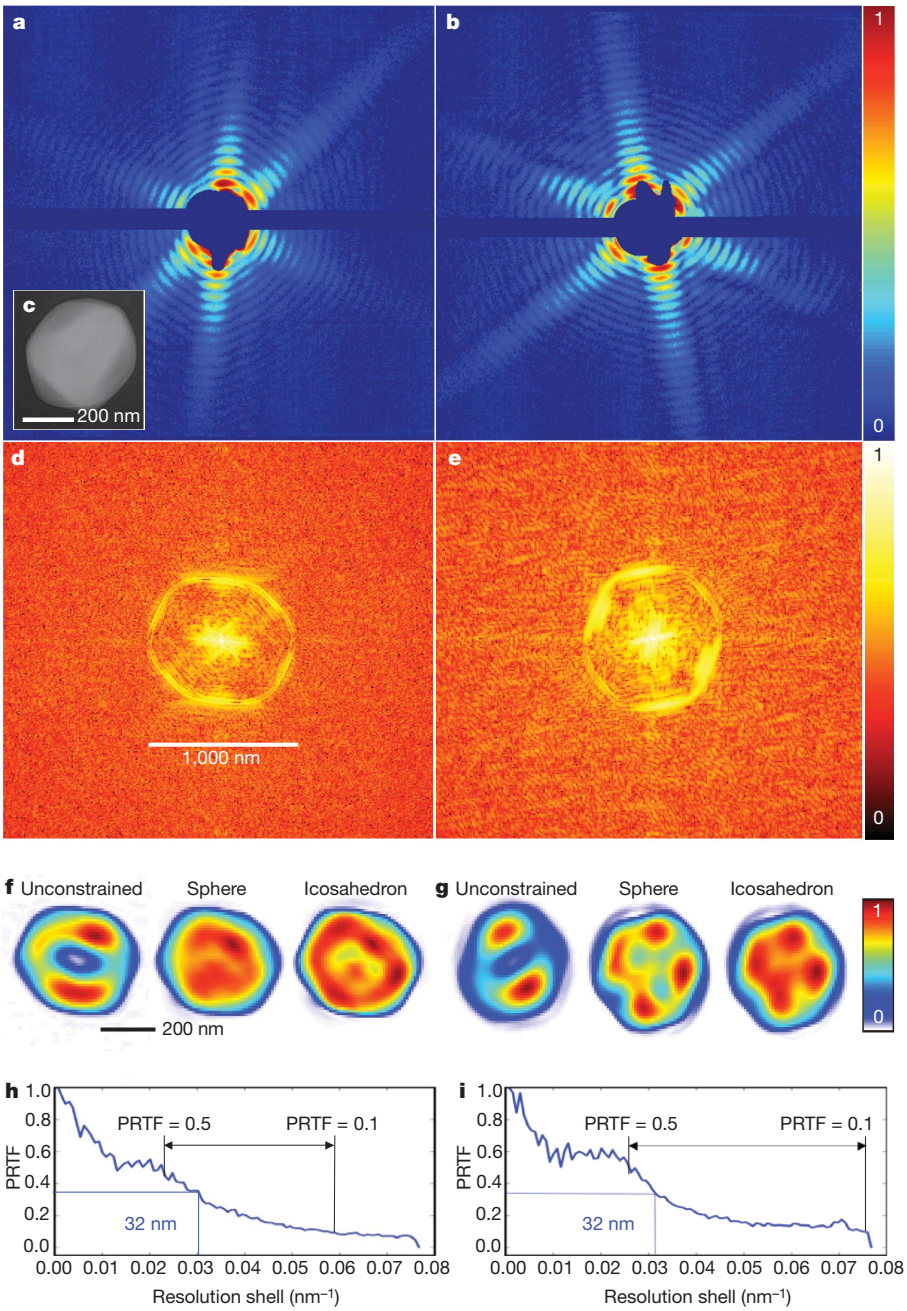


**Figure 2 | Single-shot diffraction patterns on single virus particles give interpretable results.** **a**, **b**, Experimentally recorded far-field diffraction patterns (in false-colour representation) from individual virus particles captured in two different orientations. **c**, Transmission electron micrograph of an unstained Mimivirus particle, showing pseudo-icosahedral appearance[7]. **d**, **e**, Autocorrelation functions for **a** (**d**) and **b** (**e**). The shape and size of each autocorrelation correspond to those of a single virus particle after high-pass filtering due to missing low-resolution data. **f**, **g**, Reconstructed images after iterative phase retrieval with the Hawk software package[16]. The size of a pixel corresponds to 9 nm in the images. Three different reconstructions are shown for each virus particle: an averaged reconstruction with unconstrained Fourier modes[19] and two averaged images after fitting unconstrained low-resolution modes to a spherical or an icosahedral profile, respectively. The orientation of the icosahedron was determined from the diffraction data. The results show small differences between the spherical and icosahedral fits. **h**, **i**, The PRTF for reconstructions where the unconstrained low-resolution modes were fitted to an icosahedron. All reconstructions gave similar resolutions. We characterize resolution by the point where the PRTF drops to 1/e (ref. 20). This corresponds to 32-nm full-period resolution in both exposures. Arrows mark the resolution range with other cut-off criteria found in the literature (Methods). Resolution can be substantially extended for samples available in multiple identical copies[1,25–28].

necessary improvement is to increase the dynamic range of the detectors. In our experiments, there were shots extending to significantly higher resolutions than those reported here but they contained too many saturated pixels at low angles (more missing modes), preventing image reconstruction. With reproducible samples, where the experiment can be repeated on a new object, a three-dimensional data set can be collected, and the resolution extended (even from weak individual exposures) by merging redundant data[25–29]. Studies of virus particles with higher-intensity photon pulses and improved detectors could answer the question of whether the core is reproducible to subnanometre resolution or whether the viral genome has the 'molecular individualism' that genomic DNA structures explore *in vitro*[30].

*Note added in proof*: In a previous study[31], synchrotron radiation was used to obtain X-ray diffraction data on a herpes virus.

## METHODS SUMMARY

Experiments were performed with the CAMP instrument[12] on the AMO beamline[13] at the LCLS[5], with the LCLS running at a repetition rate of 30 Hz. CAMP supports a variety of imaging and atomic/molecular physics experiments.

Diffraction patterns were recorded on a pair of pnCCD detectors[12] (maximum read-out speed, 250 frames per second). The sample-to-detector distance was 564 mm. The active area of each detector half was 76.8 mm × 38.4 mm and contained 1,024 × 512 pixels of area 75 × 75 $\mu m^2$. The full-well capacity of a pixel was 280,000 electrons, corresponding to ~570 X-ray photons per pixel at 1.8-keV photon energy.

The electron bunch was 70 fs long (full-duration at half-maximum), but the corresponding photon bunch is thought to be shorter[22]. The photon bunch contained $8 \times 10^{11}$ photons per pulse (0.24 mJ at 1.8 keV) and had a diameter of ~10 μm (full-width at half-maximum) at the interaction point, giving $\sim 1.6 \times 10^{10}$ photons per square micrometre in the centre of the beam and a peak power density of $\sim 6.5 \times 10^{15}$ W $cm^{-2}$. Background scattering from residual gas in the vacuum chamber did not exceed the read-out noise of the detectors nor the noise of the diffuse photon background (<1.3 photons per pixel). This is remarkable, considering that the number of photons in the pulse was nearly 100,000,000,000 times higher than the photon background.

Purified mimivirus was transferred into a volatile buffer and the suspension was aerosolized with helium gas in a gas dynamic nebulizer[14]. The aerosol of hydrated virus particles was sampled into a differentially pumped injector through an inlet nozzle coupled to a skimmer. The aerosol (in helium atmosphere) passed through a variable relaxation chamber from where the equilibrated and adiabatically cooled particles entered a differentially pumped aerodynamic lens stack. Particles focused by the aerodynamic lens were intercepted randomly by the LCLS pulses. Diffraction patterns of free-flying virus particles were exceptionally clean.

Image reconstruction was performed with the open source Hawk software[16], available from http://xray.bmc.uu.se/hawk. The background-corrected diffraction patterns and the Hawk configuration files used in the reconstructions can be downloaded from this site.

**Full Methods** and any associated references are available in the online version of the paper at www.nature.com/nature.

**Received 16 July; accepted 9 December 2010.**


1. Neutze, R. *et al.* Potential for biomolecular imaging with femtosecond X-ray pulses. *Nature* **406,** 752–757 (2000).
2. Chapman, H. N. *et al.* Femtosecond diffractive imaging with a soft-X-ray free-electron laser. *Nature Phys.* **2,** 839–843 (2006).
3. Bergh, M. *et al.* Feasibility of imaging living cells at sub-nanometer resolution by ultrafast X-ray diffraction. *Q. Rev. Biophys.* **41,** 181–204 (2008).
4. Nagler, B. *et al.* Turning solid aluminium transparent by intense soft X-ray photoionization. *Nature Phys.* **5,** 693–696 (2009).
5. Emma, P. *et al.* First lasing and operation of an ångstrom-wavelength free-electron laser. *Nature Photon.* **4,** 641–647 (2010).
6. La Scola, B. *et al.* A giant virus in amoebae. *Science* **299,** 2033 (2003).
7. Xiao, C. *et al.* Structural studies of the giant mimivirus. *PLoS Biol.* **7,** e1000092 (2009).
8. Claverie, J. M. & Abergel, C. Mimivirus and its virophage. *Annu. Rev. Genet.* **43,** 49–66 (2009).
9. Raoult, D. *et al.* The 1.2-megabase genome sequence of mimivirus. *Science* **306,** 1344–1350 (2004).
10. La Scola, B. *et al.* The virophage as a unique parasite of the giant mimivirus. *Nature* **455,** 100–104 (2008).
11. Claverie, J. M. & Abergel, C. Mimivirus: the emerging paradox of quasi-autonomous viruses. *Trends Genet.* **26,** 431–437 (2010).
12. Strüder, L. *et al.* Large-format, high-speed, X-ray pnCCDs combined with electron and ion imaging spectrometers in a multipurpose chamber for experiments at 4th generation light sources. *Nucl. Instrum. Methods Phys. Res. A* **614,** 483–496 (2010).
13. Bozek, J. D. AMO instrumentation for the LCLS X-ray FEL. *Eur. Phys. J. Spec. Top.* **169,** 129–132 (2009).
14. DePonte, D. P. *et al.* Gas dynamic virtual nozzle for generation of microscopic droplet streams. *J. Phys. D* **41,** 195505 (2008).
15. Bogan, M. J. *et al.* Single particle X-ray diffractive imaging. *Nano Lett.* **8,** 310–316 (2008).
16. Maia, F. R. N. C., Ekeberg, T., van der Spoel, D. & Hajdu, J. *Hawk*: the image reconstruction package for coherent X-ray diffractive imaging. *J. Appl. Crystallogr.* **43,** 1535–1539 (2010).
17. Luke, D. R. Relaxed averaged alternating reflections for diffraction imaging. *Inverse Probl.* **21,** 37–50 (2005).
18. Marchesini, S. *et al.* X-ray image reconstruction from a diffraction pattern alone. *Phys. Rev. B* **68,** 140101 (2003).
19. Thibault, P., Elser, V., Jacobsen, C., Shapiro, D. & Sayre, D. Reconstruction of a yeast cell from X-ray diffraction data. *Acta Crystallogr. A* **62,** 248–261 (2006).
20. Shapiro, D. *et al.* Biological imaging by soft X-ray diffraction microscopy. *Proc. Natl Acad. Sci. USA* **102,** 15343–15346 (2005).
21. Ding, Y. *et al.* Measurements and simulations of ultralow emittance and ultrashort electron beams in the Linac Coherent Light Source. *Phys. Rev. Lett.* **102,** 254801 (2009).
22. Young, L. *et al.* Femtosecond electronic response of atoms to ultra-intense X-rays. *Nature* **466,** 56–61 (2010).
23. Hau-Riege, S. P. *et al.* A sacrificial tamper slows down sample explosion in flash diffraction experiments. *Phys. Rev. Lett.* **104,** 064801 (2010).
24. Chapman, H. N. *et al.* Femtosecond X-ray protein nanocrystallography. *Nature* doi:10.1038/nature09750 (this issue).
25. Huldt, G., Szoke, A. & Hajdu, J. Diffraction imaging of single particles and biomolecules. *J. Struct. Biol.* **144,** 219–227 (2003).
26. Fung, R. *et al.* Structure from fleeting illumination of faint spinning objects in flight. *Nature Phys.* **5,** 64–67 (2009).
27. Loh, N. T. D. & Elser, V. Reconstruction algorithm for single-particle diffraction imaging. *Phys. Rev. E* **80,** 026705 (2009).
28. Bortel, G., Faigel, G. & Tegze, M. Classification and averaging of random orientation single macromolecular diffraction patterns at atomic resolution. *J. Struct. Biol.* **166,** 226–233 (2009).
29. Maia, F. R. N. C., Ekeberg, T., Tımneanu, N., van der Spoel, D. & Hajdu, J. Structural variability and the incoherent addition of scattered intensities in single-particle diffraction. *Phys. Rev. E* **80,** 031905 (2009).
30. Perkins, T. T., Smith, D. E. & Chu, S. Single polymer dynamics in an elongated flow. *Science* **276,** 2016–2021 (1997).
31. Song, C. *et al.* Quantitative imaging of single, unstained viruses with coherent X rays. *Phys. Rev. Lett.* **101,** 158101 (2008).


**Supplementary Information** is linked to the online version of the paper at www.nature.com/nature.

**Acknowledgements** This work was supported by the following agencies: the Swedish Research Councils; the Swedish Foundation for International Cooperation in Research and Higher Education; Stiftelsen Olle Engkvist Byggmästare; the Swedish University of Agricultural Sciences; the Helmholtz Association (VH-VI-302); the DFG Cluster of Excellence at the Munich Centre for Advanced Photonics; the Centre National de la Recherche Scientifique; Agence Nationale de la Recherche (ANR-BLAN08-0089); the Hamburg Ministry of Science and Research and Joachim Herz Stiftung, as part of the Hamburg Initiative for Excellence in Research (LEXI); the Hamburg School for Structure and Dynamics; the Max Planck Society, the US National Science Foundation (grants MCB 0919195 and MCB-1021557); and the US Department of Energy, through the PULSE Institute. Portions of this research were carried out at the Linac Coherent Light Source, a National User Facility operated by Stanford University on behalf of the US Department of Energy, Office of Basic Energy Sciences. We are grateful to B. Hedman and N. Timneanu for their help and to the scientific and technical staff of the LCLS for their outstanding facility and support.

**Author Contributions** J.H. and H.N.C. conceived the experiment. C.A., V.S., J.-M.C., M.S., O.J., A. Rocker, I.A. and D.O. prepared and characterized the samples. J.D.B., C.B. and K.O.H. created the LCLS beamline. J.H., H.N.C., J.S., L.G., A.B., N.C., A.A., A.M., J.K., K.O.H. and S.P.H.-R. developed the imaging concept. S.W.E., R.H., D. Rolles, A. Rudenko, C.S., L.F., N.K., P.H., B.R., B.E., A.H., Ch.R., D.P., G.W., L.S., G.H., H. Gorke, J.U., I.S., S.H., G.S., F.S., H.S., K.-U.K., R.A., C.-D.S., F.K., M. Bott, S. Schorb, D. Rupp, M.A., T.G., H.H., L.G., G.P., H. Graafsma and B.N. designed and set up the CAMP instrument and/or developed and operated the pnCCD detectors. S. Bajt and M. Barthelmess coordinated instrumentation, worked on engineering and prepared filters and calibration samples. J.K., S.P.H.-R., A.B., H.N.C., J.S., A.M. and N.C. characterized the focus. B.I., D.W., M.S., M.M.S. and J.H. built the sample injector. D.P.D., J.H., M.S., D.W., U.W., R.K., M. Hunter, R.B.D. and J.C.H.S. designed and built the nanospray nebulizer. J.H., M.S., M.M.S., F.R.N.C.M., J.A., A.A.M., A. Rocker, M.J.B., C.Y.H., R.G.S., S. Boutet, I.A., O.J., D.S., A.B., J.S., D.P.D., A.A., M.L., J.K., T.A.W., A.M., R.L.S., L.L., M. Barthelmess, J.C.H.S., P.F., I.S., U.W., R.K., M. Hunter, R.B.D., M.F., G.W., M. Bott, S.W.E., B.E., L.F., R.H., N.K., L.L., D. Rupp, B.R., A. Rudenko, R.L.S., L.S., I.S., C.S., J.U. and H.N.C. characterized the imaging apparatus and carried out the experiment. T.E., F.R.N.C.M., M. Hantke, M.M.S., A.B., T.A.W., A.M., A.A., S.M., M.M. and J.H. analysed the data. T.E., F.R.N.C.M., A.B. and S.M. performed image reconstructions. J.H. and T.E. wrote the manuscript with input from all authors.

**Author Information** Reprints and permissions information is available at www.nature.com/reprints. The authors declare no competing financial interests. Readers are welcome to comment on the online version of this article at www.nature.com/nature. Correspondence and requests for materials should be addressed to J.H. (janos.hajdu@xray.bmc.uu.se) or C.A. (chantal.abergel@igs.cnrs-mrs.fr).

## METHODS

**Experimental set-up at the LCLS.** Experiments were performed with the CAMP instrument[12] on the AMO beamline[13] at the LCLS[5], with the LCLS running at a repetition rate of 30 Hz. CAMP supports a variety of imaging and atomic/molecular physics experiments.

Diffraction patterns were recorded on a pair of pnCCD detectors[12] (maximum read-out speed, 250 frames per second). The sample-to-detector distance was 564 mm. The active area of each detector half was 76.8 mm × 38.4 mm and contained 1,024 × 512 pixels of area 75 × 75 μm$^2$. The full-well capacity of a pixel was 280,000 electrons, corresponding to ~570 X-ray photons per pixel at 1.8-keV photon energy.

The electron bunch was 70 fs long (full-duration at half-maximum), but the corresponding photon bunch is thought to be shorter[22]. The photon bunch contained $8 \times 10^{11}$ photons per pulse (0.24 mJ at 1.8 keV) and had a diameter of ~10 μm (full-width at half-maximum) at the interaction point, giving $\sim 1.6 \times 10^{10}$ photons per square micrometre in the centre of the beam and a peak power density of $\sim 6.5 \times 10^{15}$ W cm$^{-2}$. Background scattering from residual gas in the vacuum chamber did not exceed the read-out noise of the detectors nor the noise of the diffuse photon background (<1.3 photons per pixel). This is remarkable, considering that the number of photons in the pulse was nearly 100,000,000,000 times higher than the photon background.

Purified mimivirus[32] particles were transferred into a volatile buffer (250 mM ammonium acetate, pH 7.5) and the suspension ($10^{12}$ particles per millilitre) was aerosolized at a rate of about 5 μl min$^{-1}$, using helium gas in a gas dynamic nebulizer[14]. The aerosol of hydrated virus particles was sampled into a differentially pumped sample injector through an inlet nozzle coupled to a skimmer. Most of the nebulizing gas, and vapours of the volatile buffer, were pumped away at this point. The heavier aerosol (in a wet helium atmosphere at a pressure of about $10^{-2}$ mbar) passed through a variable-volume relaxation chamber from where the equilibrated and adiabatically cooled particles entered a differentially pumped aerodynamic lens stack. The pressure dropped from about $10^{-2}$ mbar to about $10^{-4}$ mbar at the exit of the lens. Particles focused by the aerodynamic lens entered the interaction zone ($10^{-6}$ mbar) with an estimated velocity of 60–100 m s$^{-1}$ and were intercepted randomly by the LCLS pulses.

Data processing included removal of signal from known bad or saturated pixels, correction for the residual common mode offsets and application of a flat-field correction. The corrected patterns were used directly without symmetrization.

Image reconstruction was performed with the open-source Hawk software package[16], using the RAAR algorithm[17] and its support constraint, enhanced by additional reality and positivity constraints. Hawk is available from http://xray.bmc.uu.se/hawk. The background-corrected diffraction patterns and the Hawk configuration files used in the reconstructions can be downloaded from this site.

A Fourier constraint was applied to match Fourier amplitudes with experimental amplitudes through a projection. No explicit Fourier constraints were used for regions of missing data, although these regions were implicitly constrained in Fourier space by the real-space constraints. The support was handled using a Shrinkwrap algorithm[18] with the constraint of having a specific area that was estimated from the autocorrelation function.

Weakly constrained modes in the reconstructions were identified and removed, using the formalism of ref. 19. This is a linear algebra method to compensate for noise, or the lack of constraints in the missing central region of the pattern. The diffracted amplitudes in the region of missing data can be recovered by iterative phasing algorithms, but for patterns where this region is extensive the recovered amplitudes will be unreliable[19]. Missing modes were identified and their constraining power was calculated by performing a singular-value decomposition on the transform from the region of missing data to the support. The singular values identify the modes that are most weakly constrained, as the singular vectors, and determine their constraining power. In the patterns discussed in this paper, there are modes with very low constraining power. These modes are therefore virtually unconstrained and their strength had to be estimated in another way. The threshold used for identifying unconstrained modes was 0.999, corresponding to a constraining power of 0.045. The uncertainty in the total image density dropped to less than 10% after removing these modes. Missing modes were fitted to match the total density of a spherical or a suitably rotated icosahedral profile. The missing modes were adjusted to give a total density that best matched the target.

The number of weakly constrained modes that were classified as unconstrained differs slightly between the two reconstructions because the support recovered through the Shrinkwrap algorithm[17] is slightly different for Fig. 2a and Fig. 2b. For the reconstruction starting from Fig. 2a, the median number of missing modes was 8 and the average was 7.75 modes. For the reconstruction starting from Fig. 2b, the number was slightly higher: median 12 and average 11.85. This difference is due to a larger area being missing in the centre of Fig. 2b owing to there being more saturated pixels.

Residual phase fluctuations were suppressed by averaging many reconstructions, using different random seeds. The results gave improved image reliability. For reconstructions from Fig. 2a, 10,000 iterations were used and 200 reconstructions were obtained from different random starting positions and then used to calculate the PRTF. The support was updated every 20 iterations. All 200 reconstructions had a Fourier error below a threshold of 0.33. For reconstructions from Fig. 2b, 40,000 iterations were performed and 94 reconstructions obtained. Of these, only 56 reconstructions had a Fourier error below a threshold of 0.33. The differences underline the deleterious effect of missing low-resolution data on image reconstruction. Reliable image reconstruction needs a more efficient way of measuring low-angle diffraction data, including a wider dynamic range for the detector. An attenuator disk centred on the X-ray beam and placed over the middle part of the pnCCD detector pair could reduce the strong forward-scattered signal in the middle of the diffraction pattern and bring low-resolution data within the useful dynamic range of the detector.

We estimate the image resolution in the reconstruction by computing the PRTF[2,20]. No consensus has emerged so far on what single PRTF value should be used as the measure of resolution. Values between 0.5 and 0.1 can be found in the literature[33]. We characterize resolution by the point where the PRTF drops to 1/e (ref. 20). Diffraction data extend to higher resolution than the resolution given by the PRTF.

The angle spanned by the signal was small enough for the entire particle to fit within the depth of field. Defocus effects are therefore avoided by using a reality constraint. A resolution of 1 nm at the same X-ray wavelength would require measuring at high angle, leading to significant deviation from the projection image. Real-value constraints would not work in the latter case, and this would make the reconstruction more challenging but by no means impossible (see, for example, ref. 34).

Transmission electron microscopy was performed with a Hitachi H-7100 electron microscope on unstained mimivirus particles deposited on Formvar-coated gold grids.

**A route for improvements.** There is a clear need to achieve higher resolution in single shots. This requires an increased photon flux on the sample as well as a wider dynamic range for detecting photons in the diffraction pattern. The LCLS[5] is capable of delivering very short X-ray pulses[21] to outrun significant sample explosion with more photons per pulse. Tighter focusing and an increased photon output from the LCLS have already been achieved and will increase the flux on the samples in forthcoming runs. A broad dynamic range in detecting photons is necessary to avoid saturation at low angles. In this first set of experiments, there were already exposures with significantly higher resolutions than those reported here, but these exposures contained too many saturated pixels at low angles, preventing image reconstruction. Reliable image reconstruction needs a more efficient way of measuring low-angle diffraction data. A graded attenuator around the central hole of the pnCCD detector pair could help here. An additional pair of detectors placed far behind the first detector pair could record more of the low-angle data over a larger area. Maintaining sample integrity during injection is a key requirement in the experiment. More data on a diverse set of samples (such as cells, viruses and macromolecules) will be needed to map out the available parameter space. Hit rates could be increased by improved injection methods, using a narrower particle beam. A future extension to imaging single macromolecules will need these developments.


32. Byrne, D. *et al.* The polyadenylation site of Mimivirus transcripts obeys a stringent 'hairpin rule'. *Genome Res.* **19,** 1233–1242 (2009).
33. Steinbrener, J. *et al.* Data preparation and evaluation techniques for X-ray diffraction microscopy. *Opt. Express* **18,** 18598–18614 (2010).
34. Seibert, M. M. *et al.* Femtosecond diffractive imaging of biological cells. *J. Phys. At. Mol. Opt. Phys.* **43,** 194015 (2010).